

Modeling H_2 formation in the turbulent ISM: Solenoidal versus compressive turbulent forcing

Milica Micic^{1*}, Simon C. O. Glover¹, Christoph Federrath^{1,2,3} and Ralf S. Klessen¹

¹*Zentrum für Astronomie der Universität Heidelberg, Institut für Theoretische Astrophysik, Albert-Ueberle-Str. 2, 69120 Heidelberg*

²*Ecole Normale Supérieure de Lyon, CRAL, 69364 Lyon, France*

³*Monach Centre for Astrophysics (MoCA), School of Mathematical Sciences, Monach University, Vic 3800, Australia*

15 January 2013

ABSTRACT

We present results from high-resolution three-dimensional simulations of the turbulent interstellar medium that study the influence of the nature of the turbulence on the formation of molecular hydrogen. We have examined both solenoidal (divergence-free) and compressive (curl-free) turbulent driving, and show that compressive driving leads to faster H_2 formation, owing to the higher peak densities produced in the gas. The difference in the H_2 formation rate can be as much as an order of magnitude at early times, but declines at later times as the highest density regions become fully molecular and stop contributing to the total H_2 formation rate. We have also used our results to test a simple prescription suggested by Gnedin et al. (2009) for modeling the influence of unresolved density fluctuations on the H_2 formation rate in large-scale simulations of the ISM. We find that this approach works well when the H_2 fraction is small, but breaks down once the highest density gas becomes fully molecular.

Key words: astrochemistry – molecular processes – ISM: clouds – ISM: molecules – methods: numerical – turbulence.

1 INTRODUCTION

All observed Galactic star formation takes place within dense, massive clouds of molecular gas known as giant molecular clouds (GMCs). Understanding how these clouds form and evolve is therefore a crucial part of the study of star formation on galactic scales. In the past, molecular clouds have been seen as quasi-static objects that form stars slowly over a long lifetime where the dynamical evolution of a cloud and the chemical evolution of the gas within it were only loosely coupled and were modeled separately. However, observations provide velocity dispersions documenting the existence of supersonic random motions on scales larger than ~ 0.1 pc (e.g. Goldreich & Kwan 1974; Zuckerman & Evans 1974; Larson 1981; Myers 1983; Péroult et al. 1986; Solomon et al. 1987; Falgarone et al. 1992; Ossenkopf & Mac Low 2002; Heyer & Brunt 2004; Roman-Duval et al. 2011; Schneider et al. 2011). These motions have been associated with compressible turbulence in the interstellar medium (ISM) leading to appreciation that GMCs are highly inhomogeneous and that their formation and evolution are dominated by the effects of supersonic turbulent mo-

tions (Ballesteros-Paredes, Hartmann & Vázquez-Semadeni 1999; Mac Low & Klessen 2004; Elmegreen & Scalo 2004; Scalo & Elmegreen 2004). The dynamical evolution of the clouds is rapid, with a timescale comparable to those of the most important chemical processes such as the conversion of atomic to molecular hydrogen or the freeze-out of molecules onto the surfaces of interstellar dust grains. In this picture, the dynamics and chemistry of the gas are strongly coupled, with one directly influencing the evolution of the other, meaning that they must be modeled together.

The main chemical constituent of the molecular gas is molecular hydrogen, H_2 , with other molecules such as CO being present only in small amounts, so in practice the study of the formation of molecular gas is usually simply the study of the formation of H_2 . The molecule forms in the interstellar medium primarily on the surface of dust grains. Its formation in the gas phase by radiative association is highly forbidden due to the molecule's lack of a permanent dipole moment and occurs at a negligibly slow rate (Gould & Salpeter 1963), while the gas phase formation via intermediate molecular ions such as H^- or H_2^+ is strongly suppressed by the interstellar radiation field (Glover 2003) and cannot produce molecular fractions much higher than $x_{\text{H}_2} \simeq 10^{-3}$.

Given the relatively slow rate at which H_2 forms, it is natural to ask whether it is possible to produce large

* E-mail: milica@uni-hd.de

amounts of H_2 quickly enough for a model involving rapid cloud formation to be viable. Glover & Mac Low (2007b) have shown that dynamical processes such as supersonic turbulence have a great impact on the effective H_2 formation rate. The presence of turbulence dramatically reduces the time required to form large quantities of H_2 . The density compressions created by supersonic turbulence allow H_2 to form rapidly, with large molecular fractions being produced after only 1–2 Myr, consistent with the timescale required by rapid cloud formation models. It is found that much of the H_2 is formed in high density gas and then transported to lower densities by the action of the turbulence (Federrath et al. 2008a), a phenomenon that certainly has a significant impact on the chemistry of the ISM.

One issue not addressed in the study by Glover & Mac Low (2007b) was the sensitivity of these results to the nature of the turbulent velocity field. Most of the work that has been done to date on the numerical modeling of molecular cloud turbulence has focussed on either purely solenoidal (i.e. divergence-free) turbulence, or weakly compressive turbulence where the solenoidal modes dominate over the compressive (curl-free) modes (see e.g. Klessen, Heitsch & Mac Low 2000; Klessen 2001; Ostriker, Stone & Gammie 2001; Lemaster & Stone 2008). The study by Glover & Mac Low (2007b) is no exception, as it used the same setup for generating weakly compressive turbulence as in earlier work by Mac Low et al. (1998) and Mac Low (1999). Recently, however, Federrath and collaborators have performed a number of studies of fully compressive turbulence (Federrath et al. 2008b, 2009; Schmidt et al. 2009; Federrath et al. 2010). They show that compressive turbulence produces a significantly broader spread of densities than solenoidal turbulence with the standard deviation of the density probability distribution functions (PDFs) differing by a factor of 3 at the same rms Mach number and argue that while solenoidal forcing of turbulence is likely to occur in quiescent regions with low star formation rates like in the Polaris Flare and or Maddalena’s Cloud, regions with a higher star formation activity are more compatible with compressive turbulence (see also, Federrath et al. 2010; Brunt 2010; Price, Federrath & Brunt 2011).

The influence of the wide spread of densities produced by compressively driven turbulence on the rate at which molecular hydrogen forms in the ISM has not previously been investigated, but given the strong density dependence of the H_2 formation rate, it is plausible that the effect could be large. To address this issue, we have carried out a numerical investigation of the rate at which H_2 forms in interstellar gas dominated by compressive turbulence, and how this compares to the H_2 formation rate in gas dominated by solenoidal turbulence.

The outline of our paper is as follows. In §2 we describe our numerical method, paying particular attention to the treatment of chemistry and cooling, as well as the method used to generate and maintain turbulence in the gas. In §3 we present our results for the H_2 formation rate, and discuss the distributions of density, temperature and H_2 abundance generated in the simulations. We also use our results to test the sub-grid scale model for H_2 formation in turbulent gas put forward by Gnedin et al. (2009). We close with a summary of our findings in section 4.

2 SIMULATIONS

2.1 Numerical method

2.1.1 Chemistry and cooling

Modeling the thermal evolution of the gas in a meaningful fashion and having a full chemical model of the ISM can easily require one to track several hundred different atomic and molecular species involved in several thousand different reactions, even if reactions on grain surfaces are neglected (see e.g. the UMIST Database for Astrochemistry, as described in Woodall et al. 2007). This is impractical to include in a 3D hydrodynamical code, since it would have an extreme impact on the code’s performance. In order to run time-dependent chemical networks efficiently alongside the dynamical evolution of the system one needs to select a number of chemical species and mutual reactions such that the chemical network can be solved in a short enough time while still adequately describing the overall evolution of the system (see Glover & Mac Low 2007a,b). For our purposes we need to be able to follow the formation and destruction of H_2 with a reasonable degree of accuracy.

We have modified the FLASH v2.5 adaptive mesh refinement code (Fryxell et al. 2000; Calder et al. 2002) to include a detailed atomic/molecular cooling function and a simplified but accurate treatment of the most important hydrogen chemistry. FLASH is a massively parallel code, developed by the Center for Astrophysical Thermonuclear Flashes at the University of Chicago. It has support for a variety of different physical processes, including magneto-hydrodynamical (MHD) flows and self-gravity. FLASH uses the PARAMESH library to manage a block-structured adaptive grid and the Message-Passing Interface (MPI) for parallelization.

Our modifications add a limited treatment of non-equilibrium chemistry treated in an operator-split fashion (Glover & Mac Low 2007a,b). During each hydro step, the coupled set of chemical rate equations for the fluid are solved using the implicit integrator DVODE (Brown, Byrne & Hindmarsh 1989), together with the portion of the internal energy equation dealing with compressional and radiative heating and cooling, under the assumption that the other hydrodynamical variables (e.g. density) remain fixed. The advection of the gas energy density is handled as in the unmodified FLASH code. Chemical abundances are tracked using FLASH’s standard tracer field implementation, and consistent multifluid advection (Plewa & Müller 1999) is used to reduce the advection errors.

By default, the internal energy in FLASH is computed by subtracting the specific kinetic energy from the total specific energy, using the equation

$$\varepsilon = E - \frac{|\mathbf{v}|^2}{2}, \quad (1)$$

where ε is the specific internal energy, E is the specific total energy and \mathbf{v} is the velocity. In regions where the kinetic energy greatly dominates the total energy due to truncation error this approach can lead to unphysical (e.g. negative) internal energies, giving inaccurate values for pressures and temperatures. This problem can be avoided by evolving the internal energy separately, using the equation

Table 1. Reactions in our non-equilibrium chemical model.

No.	Reaction	Reference
1	$\text{H} + \text{H} + \text{grain} \rightarrow \text{H}_2 + \text{grain}$	1
2	$\text{H}_2 + \text{H} \rightarrow \text{H} + \text{H} + \text{H}$	2
3	$\text{H}_2 + \text{H}_2 \rightarrow \text{H} + \text{H} + \text{H}_2$	3
4	$\text{H}_2 + \text{e}^- \rightarrow \text{H} + \text{H} + \text{e}^-$	4
5	$\text{H} + \text{c.r.} \rightarrow \text{H}^+ + \text{e}^-$	See §2.2
6	$\text{H}_2 + \text{c.r.} \rightarrow \text{H} + \text{H}$	See §2.2
7	$\text{H}_2 + \text{c.r.} \rightarrow \text{H} + \text{H}^+ + \text{e}^-$	See §2.2
8	$\text{H} + \text{e}^- \rightarrow \text{H}^+ + \text{e}^- + \text{e}^-$	5
9	$\text{H}^+ + \text{e}^- \rightarrow \text{H} + \gamma$	6
10	$\text{H}^+ + \text{e}^- + \text{grain} \rightarrow \text{H} + \text{grain}$	7

References: 1: Hollenbach & McKee (1979), 2: Mac Low & Shull (1986), 3: Martin, Keogh & Mandy (1998), 4: Trevisan & Tennyson (2002), 5: Abel et al. (1997), 6: Ferland et al. (1992), 7: Weingartner & Draine (2001)

$$\frac{\partial \rho \varepsilon}{\partial t} + \nabla \cdot [(\rho \varepsilon + P)\mathbf{v}] - \mathbf{v} \cdot \nabla P = 0, \quad (2)$$

where ρ is the density and P is the gas pressure. The method used within the FLASH code is determined via the runtime parameter *eint_switch*. If the internal energy is smaller than *eint_switch* times the kinetic energy, then the total energy is recomputed using the internal energy from Eq. 2 and the velocities from the momentum equation. We have found that by setting *eint_switch* = 10^{-4} , we are able to avoid any problems due to truncation error.

We treat the cooling coming from metals by assuming that the carbon, oxygen and silicon in the gas remain in the form of C^+ , O and Si^+ , respectively, as in the previous studies of Glover & Mac Low (2007a,b). In practice, in the absence of photodissociating radiation (see below), we would expect carbon and silicon to rapidly recombine, and for the carbon to be converted to CO once the H_2 fraction becomes large. However, we know from previous work (Glover & Clark 2011a,b) that the behaviour of the gas is not particularly sensitive to whether the dominant coolant is C^+ or CO. Cooling from C^+ alone can reduce the gas temperature to values around 15–20 K, and although CO cooling enables the gas to reach even lower temperatures ($T \sim 10$ K), in realistic models of GMCs, the characteristic temperature of the fully molecular gas is generally in the range of 10 – 20 K (Glover & Clark 2011b). As the H_2 formation rate does not have a strong dependence on temperature, the approximate nature of our thermal treatment will have little influence on the H_2 formation rate in the gas. However, making this simplification allows us to minimize the computational requirements for our simulations by using a considerably simplified chemistry that follows only four species: free electrons, H^+ , H , and H_2 . We follow directly the fractional abundances of molecular hydrogen x_{H_2} and ionized hydrogen x_{H^+} (where these symbols denote the fraction of the available hydrogen found in these forms) by adding to the FLASH code an extra field variable for the mass density of each species. The abundances of the other two species - atomic hydrogen (x_{H}) and electrons (x_{e}) - are computed from the two conservation laws: conservation of charge

$$x_{\text{e}} = x_{\text{H}^+} + x_{\text{C}^+} + x_{\text{Si}^+} \quad (3)$$

Table 2. Processes included in our thermal model.

Process	Reference
C^+ fine structure cooling	Glover & Mac Low (2007a)
O fine structure cooling	Glover et al. (2010)
Si^+ fine structure cooling	Glover & Mac Low (2007a)
H_2 rovibrational lines	Glover & Abel (2008)
Gas-grain energy transfer	Hollenbach & McKee (1989)
Recombination on grains	Wolfire et al. (2003)
Atomic resonance lines	Sutherland & Dopita (1993)
H collisional ionization	Abel et al. (1997)
H_2 collisional dissociation	See Table 1
H_2 formation on dust grains	Hollenbach & McKee (1989)
Cosmic ray ionization	Goldsmith & Langer (1978)

and conservation of the number of hydrogen nuclei

$$x_{\text{H}} = x_{\text{H,tot}} - x_{\text{H}^+} - x_{\text{H}_2} \quad (4)$$

where $x_{\text{H,tot}}$ is the total abundance of hydrogen nuclei in all forms, and x_{C^+} and x_{Si^+} are the abundances of ionized carbon and silicon, respectively, which remain fixed throughout the simulations. These species undergo the reactions listed in Table 1. The radiative and chemical heating and cooling of the gas is modeled with a cooling function that contains contributions from the processes listed in Table 2.

We have also modified our treatment of the adiabatic index γ . Boley et al. (2007) have recently pointed out that as the temperature of molecular gas increases, its specific heat capacity at constant volume, c_v , changes due to the fact that first the rotational and then the vibrational energy levels of H_2 become populated and that therefore c_v cannot be considered constant and independent of temperature as has been often assumed in previous numerical studies of star formation. For this reason, we use a set of lookup tables constructed with the assumption that the H_2 ortho-to-para ratio has its thermal equilibrium value. In these tables, the specific internal energy ε is tabulated as a function of temperature T and fractional abundance of H_2 (x_{H_2}), T is tabulated as a function of ε and x_{H_2} , and the adiabatic index γ is tabulated as a function of ε (or T) and x_{H_2} . To compute the required values for γ or convert from ε to T (or vice versa), we interpolate between the values stored in the tables.

To test our modified version of the FLASH code, we performed static and turbulent simulations using both our new FLASH implementation and our existing ZEUS-MP implementation (Glover & Mac Low 2007a,b) of the same physics, and verified that the codes produced comparable results.

2.1.2 Turbulent driving and hydrodynamics

We have applied our chemistry model to simulations of forced supersonic turbulence driven by fully solenoidal (divergence-free or rotational) and fully compressive (curl-free or dilatational) forcing (Federrath et al. 2008b, 2009, 2010), as two limiting cases to investigate the influence of the nature of the driving on the formation of H_2 . These simulations use the piecewise parabolic method (PPM) (Colella & Woodward 1984) implementation of the FLASH code to integrate the equations of hydrodynamics on 3D periodic uniform grids with 256^3 grid points.

As a control parameter in our simulations, we use the rms velocity of the turbulence. We use this in preference to the rms Mach number because the latter quantity depends on the sound speed of the gas, and in our non-isothermal simulations this is not constant, but varies in both space and time. To excite a turbulent flow with a specified rms turbulent velocity, we include a forcing term \mathbf{f} in the gas momentum equation

$$\frac{\partial \mathbf{v}}{\partial t} + (\mathbf{v} \cdot \nabla) \mathbf{v} = -\frac{\nabla P}{\rho} + \mathbf{f}. \quad (5)$$

We model the random correlated stochastic forcing term \mathbf{f} such that it varies smoothly in space and time using the Ornstein-Uhlenbeck (OU) process. The OU process is a well-defined stochastic process with a finite autocorrelation timescale T . It describes the evolution of the forcing term \hat{f} in Fourier space (k -space) with the stochastic differential equation:

$$d\hat{f}(k, t) = f_0(k) \mathcal{P}^\zeta(k) dW(t) - \hat{f}(k, t) \frac{dt}{T} \quad (6)$$

where $W(t)$ is a Wiener process, a random process that adds a Gaussian random increment to the vector field given in the previous time step dt , followed by the projection tensor $\mathcal{P}^\zeta(k)$ in Fourier space. The projection operator reads

$$\mathcal{P}_{ij}^\zeta(k) = \zeta \mathcal{P}_{ij}^\perp(k) + (1 - \zeta) \mathcal{P}_{ij}^\parallel(k) = \zeta \delta_{ij} + (1 - 2\zeta) \frac{k_i k_j}{|k|^2}, \quad (7)$$

where δ_{ij} is the Kronecker symbol, and $\mathcal{P}_{ij}^\perp = \delta_{ij} - k_i k_j / k^2$ and $\mathcal{P}_{ij}^\parallel = k_i k_j / k^2$ are the fully solenoidal and the fully compressive projection operators, respectively (see e.g. Schmidt et al. 2009; Federrath et al. 2010).

By changing the value of the parameter ζ , we can determine the power of the compressive modes with respect to the total forcing power. For $\zeta = 1$ in the projection operator, we obtain a purely solenoidal force field, and with $\zeta = 0$, we obtain a purely compressive force field. Any combination of solenoidal and compressive modes can be constructed by choosing $\zeta \in [0, 1]$.

The large-scale stochastic forcing that we use, as the one closest to the observational data (Ossenkopf & Mac Low 2002; Brunt et al. 2009), models the kinetic energy input from large-scale turbulent fluctuations, breaking up into smaller structures. We thus drive the modes $k = [1, 3]$ in units of $\frac{2\pi}{L}$, where L is the box size. The forcing amplitude $A(k)$ has a parabolic dependence on k , such that most power is injected at $|\vec{k}| = 2$ and $A(1) = A(3) = 0$.

2.2 Initial conditions

Using the forcing module described above, and starting from zero velocities, we excite turbulent motions in a box with 256^3 grid points and of side length $L = 20$ pc, filled with initially uniform atomic gas, using periodic boundary conditions. We perform purely hydrodynamical simulations, and neglect any complications introduced by magnetic fields or the effects of self-gravity. The abundances for carbon, oxygen and silicon were taken from Sembach et al. (2000) and are: $x_{C+} = 1.41 \times 10^{-4}$, $x_O = 3.16 \times 10^{-4}$ and $x_{Si+} = 1.5 \times 10^{-5}$. We assume that the dust-to-gas ratio has the standard solar value, and fix the dust temperature at 10 K in every run.

We adopt a rate $\zeta_H = 10^{-17} \text{ s}^{-1}$ for the cosmic ray ionization of atomic hydrogen (reaction 5 in Table 1). In the case of molecular hydrogen, we assume that all of the H_2^+ ions produced in the reaction



are destroyed by dissociative recombination, yielding two hydrogen atoms, and so adopt a rate $\zeta_{\text{H}_2,6} = 2.22 \zeta_H$ for reaction 6 that includes this contribution as well as that coming from direct dissociation of the H_2 . For reaction 7, we adopt the rate $\zeta_{\text{H}_2,7} = 0.037 \zeta_H$. In both cases, we assume that the ratio between the H_2 destruction rates and the ionization rate of atomic hydrogen is the same as given in Woodall et al. (2007).

We perform two sets of simulations with different initial number densities: $n_0 = 30 \text{ cm}^{-3}$ and $n_0 = 300 \text{ cm}^{-3}$. For each initial density, we perform simulations with rms turbulent velocities of 0.4 km s^{-1} , 2 km s^{-1} or 4 km s^{-1} , and examine both purely solenoidal and purely compressive forcing in each case, meaning that we perform a total of twelve simulations. We evolve each simulation for ten dynamical times $T = L/2v_{\text{rms}}$. For the first two dynamical times, the chemistry module is switched off, and the turbulence is allowed to reach a statistically steady state (Federrath et al. 2009, 2010; Price & Federrath 2010). After that, we consider the chemical evolution and follow the gas for a further eight dynamical times. Note also that in our later discussion of the time evolution of the H_2 fraction, we take the time at which we switch on the chemistry module to be $t = 0$, meaning that the simulations run from $t = -2T$ until $t = 8T$.

For simplicity, we set the ambient radiation field strength to zero in all of our simulations, thereby avoiding the necessity of modeling the penetration of Lyman-Werner band photons into the simulation volume, and allowing us to focus purely on the influence of the turbulent density enhancements on the overall H_2 formation rate. We note that the mean column density through our low n_0 simulations is approximately $20 \text{ M}_\odot \text{ pc}^{-2}$, which is more than sufficient to adequately shield the H_2 in the gas against photodissociation (Krumholz et al. 2009), provided that the incident radiation field is close to the standard Galactic value. We have shown in other work (Glover & Mac Low 2011) that H_2 formation in clouds with surface densities of this value or higher is primarily limited by the time required to form the H_2 , rather than by the influence of UV photodissociation. We therefore would not expect this omission to have a large impact on our results. At late times, we will tend to under-predict the amount of atomic hydrogen in the gas, and to over-predict the amount of H_2 , particularly in our low density runs, but previous work suggests that the effect will be small (Glover & Mac Low 2011). We note, however, that this approximation will break down for clouds immersed in UV radiation fields that are significantly stronger than the standard Galactic value (Glover, in preparation).

2.3 Numerical resolution

Glover & Mac Low (2007b) and Mac Low & Glover (2010) examined the sensitivity of the H_2 formation timescale in simulations of the turbulent ISM to the numerical resolution of the simulation, using numerical resolutions ranging from

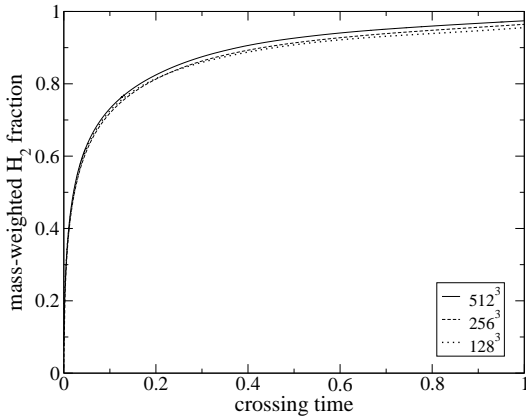


Figure 1. Time evolution of the mass-weighted H_2 abundance in units of the turbulent crossing time for $n_0 = 300 \text{ cm}^{-3}$ and $v_{\text{rms}} = 4 \text{ km s}^{-1}$ in simulations with numerical resolutions of 128^3 grid points (dotted), 256^3 grid points (dashed) and 512^3 grid points (solid).

64^3 to 512^3 zones. They found that there was some dependence on the numerical resolution of the simulation at early times, owing to the ability of the higher resolution to better model the details of the highest density structures formed by the turbulence (see Federrath et al. 2010; Price & Federrath 2010), although it should be noted that in these simulations the turbulence was not driven to a statistical steady-state before the switch-on of the chemistry, which will tend to exacerbate any resolution dependence. These previous studies found that although there remain some signs of resolution-dependence at 256^3 zones, the difference between the 128^3 , 256^3 and 512^3 results is very small. However, these resolution tests were performed only for the case of solenoidal turbulence. Therefore, to test the sensitivity of H_2 formation to numerical resolution in the simulations with compressively driven turbulence, we have performed a resolution study for the run with $v_{\text{rms}} = 4 \text{ km s}^{-1}$ and $n_0 = 300 \text{ cm}^{-3}$. This is the run in which the highest densities are produced, and so if this is well-resolved, then it is reasonable to assume that our lower density and lower v_{rms} runs will also be well-resolved. In our resolution study, we performed simulations with resolutions of 128^3 , 256^3 , and 512^3 grid cells.

In Figure 1, we show how the mass-weighted mean abundance of H_2 (defined in section 3.1 below) evolves in runs with different resolution during the first crossing time. We see that there is almost no difference in the evolution of the H_2 abundance in the three simulations, and conclude that a numerical resolution of 256^3 grid cells should be enough to accurately model the growth of the H_2 fraction in our simulations.

3 RESULTS

3.1 Time dependence of H_2 abundance

To quantify the rate at which H_2 forms in our simulation we compute the mass-weighted mean molecular fraction, $\langle x_{\text{H}_2} \rangle_{\text{M}}$, given by

$$\langle x_{\text{H}_2} \rangle_{\text{M}} = \frac{\sum_{i,j,k} \rho_{\text{H}_2}(i,j,k) \Delta V(i,j,k)}{M_{\text{H}}} \quad (9)$$

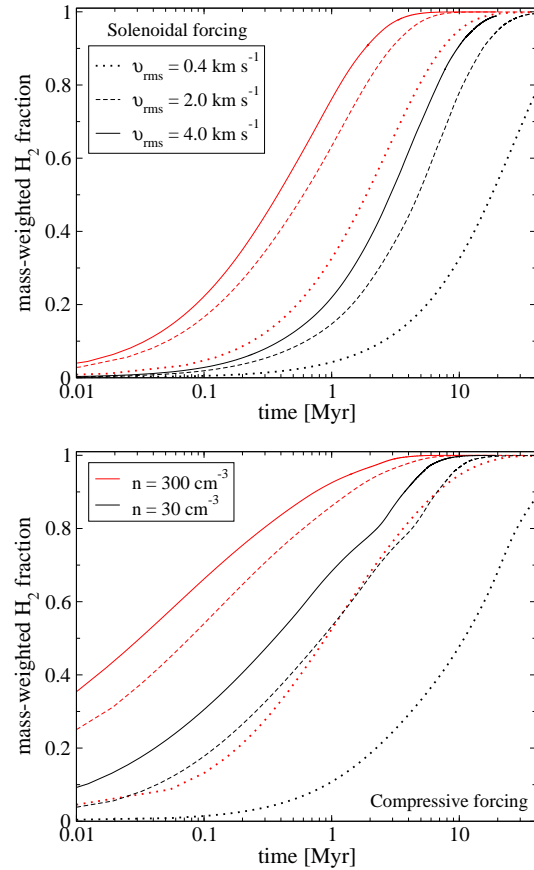


Figure 2. Evolution with time of the mass-weighted mean H_2 fraction $\langle x_{\text{H}_2} \rangle_{\text{M}}$ in runs with mean densities of 30 cm^{-3} (black) and 300 cm^{-3} (red). Three different values of the rms turbulent velocity v_{rms} are considered: 0.4 km s^{-1} (dotted), 2 km s^{-1} (dashed) and 4 km s^{-1} (solid). The upper panel shows the results for purely solenoidal forcing, while the lower panel shows the results for purely compressive forcing.

where we sum over all grid cells, and where $\rho_{\text{H}_2}(i,j,k)$ is the mass density of H_2 in computational cell (i,j,k) , $\Delta V(i,j,k)$ is the volume of the cell (i,j,k) , M_{H} is the total mass of hydrogen present in the simulation. In Figure 2, we plot the evolution of $\langle x_{\text{H}_2} \rangle_{\text{M}}$ as a function of time for both sets of runs, comparing different mean densities, rms velocities and types of driving. In Table 3, we give the time in Myr required for the mass-weighted mean molecular fraction to reach 50% ($t_{50\%}$) and 90% ($t_{90\%}$).

Looking at the evolution of H_2 fraction with time in Figure 2, we see that the time required to convert a large fraction of the initial atomic hydrogen to molecular hydrogen decreases as we increase the density or the strength of turbulent driving, in line with the previous findings of Glover & Mac Low (2007b). Comparing the two panels, we see that compressively-driven turbulence leads to more rapid formation of H_2 than turbulence driven by solenoidal forcing. The difference is particularly pronounced at early times, and in runs with high rms velocities: for instance, $t_{50\%}$ is roughly a factor of ten smaller in the compressive run with $v_{\text{rms}} = 4 \text{ km s}^{-1}$ and $n_0 = 300 \text{ cm}^{-3}$ than in the corresponding solenoidal run. At later times, the differences between the compressive and solenoidal runs become much smaller,

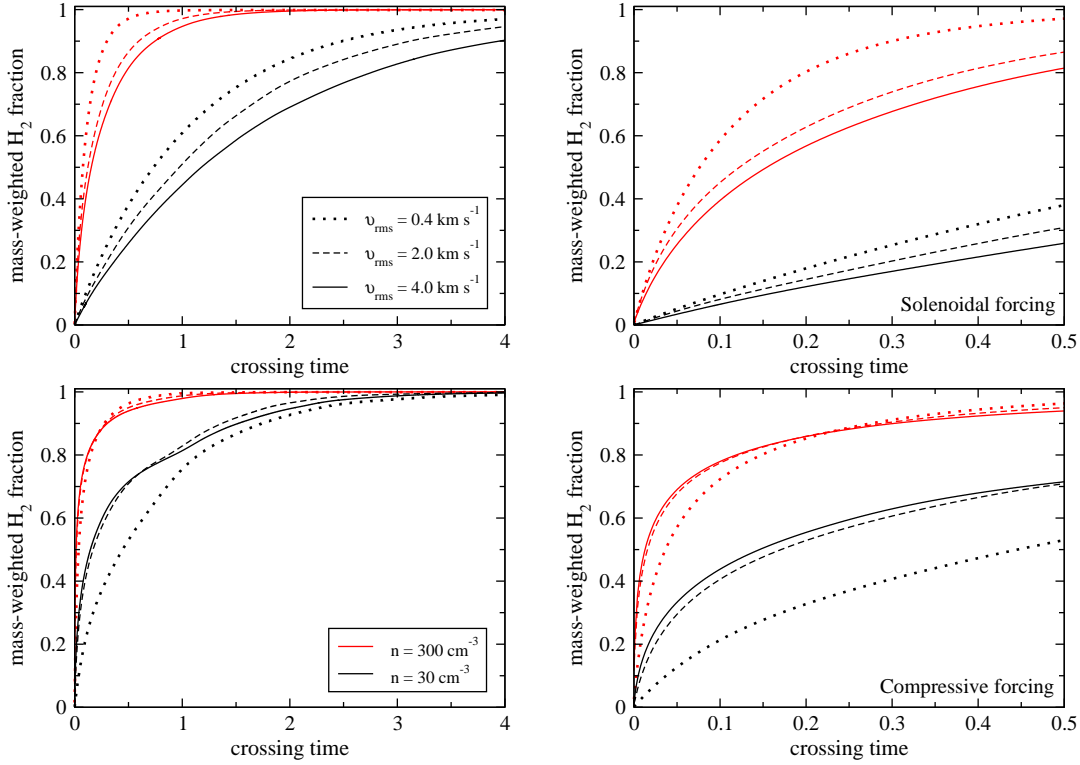


Figure 3. As Figure 2, but showing the evolution of $\langle x_{\text{H}_2} \rangle_{\text{M}}$ as a function of the turbulent crossing time T , rather than the absolute time. The left-hand panels show the evolution of $\langle x_{\text{H}_2} \rangle_{\text{M}}$ from $t = 0$ to $t = 4T$, while the right-hand panels zoom in on the period between $t = 0$ and $t = 0.5T$. As before, we plot results for three different values of the rms turbulent velocity – 0.4 km s^{-1} (dotted), 2 km s^{-1} (dashed) and 4 km s^{-1} (solid) – and two different mean densities – 30 cm^{-3} (black) and 300 cm^{-3} (red).

with $t_{90\%}$ varying by less than a factor of three even in the most turbulent runs.

In Figure 3, we show the evolution of the mass-weighted mean H_2 abundance as a function of the turbulent crossing time. Here we see that most of the dependence on the rms velocities vanishes when the time is measured in units of the crossing time. Regardless of the strength of the turbulence or the nature of the forcing, the molecular fraction reaches 50% within only $0.1 - 0.2$ crossing times in the high density model. For the low density case it takes approximately $0.5 - 1.0$ crossing times to form the same amount of molecular gas, regardless of v_{rms} .

Larger rms velocities yield more dense gas, resulting in a broader density PDF. On the other hand, they also lead to shorter turbulent crossing times, leaving less time for H_2 to form. As shown in Figure 3, these two effects largely compensate for each other. In the solenoidal case, the latter effect dominates, and the H_2 formation timescale, in units of the crossing time, decreases with decreasing v_{rms} . In runs with compressive forcing, on the other hand, the increased width of the density PDF with increasing v_{rms} is the dominant effect.

3.2 Density and temperature distributions

As Table 3 demonstrates, the H_2 formation time does not scale linearly with changes in the density of the gas. We find that an increase in density by a factor of ten causes the gas to become 90% molecular only 5 – 8 times faster in

Table 3. Time in Myr when the gas becomes 50% and 90% molecular in all our runs.

Initial number density	$n_0 = 30 \text{ cm}^{-3}$		$n_0 = 300 \text{ cm}^{-3}$	
Solenoidal forcing	$t_{50\%}$	$t_{90\%}$	$t_{50\%}$	$t_{90\%}$
$v_{\text{rms}} = 0.4 \text{ km s}^{-1}$	17.94	60.97	1.91	7.36
$v_{\text{rms}} = 2.0 \text{ km s}^{-1}$	4.79	15.30	0.64	2.96
$v_{\text{rms}} = 4.0 \text{ km s}^{-1}$	2.88	9.67	0.38	1.83
Compressive forcing	$t_{50\%}$	$t_{90\%}$	$t_{50\%}$	$t_{90\%}$
$v_{\text{rms}} = 0.4 \text{ km s}^{-1}$	10.95	42.73	0.9	6.74
$v_{\text{rms}} = 2.0 \text{ km s}^{-1}$	0.87	6.74	0.11	1.44
$v_{\text{rms}} = 4.0 \text{ km s}^{-1}$	0.36	3.73	0.036	0.74

the solenoidal case and 4 – 6 times faster in the compressive case for the same rms turbulent velocities. The reason we see less dependence than one might naively expect is clear if we look at how the density distribution varies as we change the mean density n_0 . In Figure 4 we plot a volume-weighted number density PDF at $t = 0.5$ crossing times. As we decrease the density, the entire PDF moves to low densities. Most of the H_2 forms in dense gas, and so it is not surprising that reducing the amount of dense gas available has a significant effect on x_{H_2} . However, the densest gas quickly becomes fully molecular and thereafter does not contribute to the total H_2 formation rate (see Fig. 5), reducing the effect of density increase on the amount of formed H_2 . We

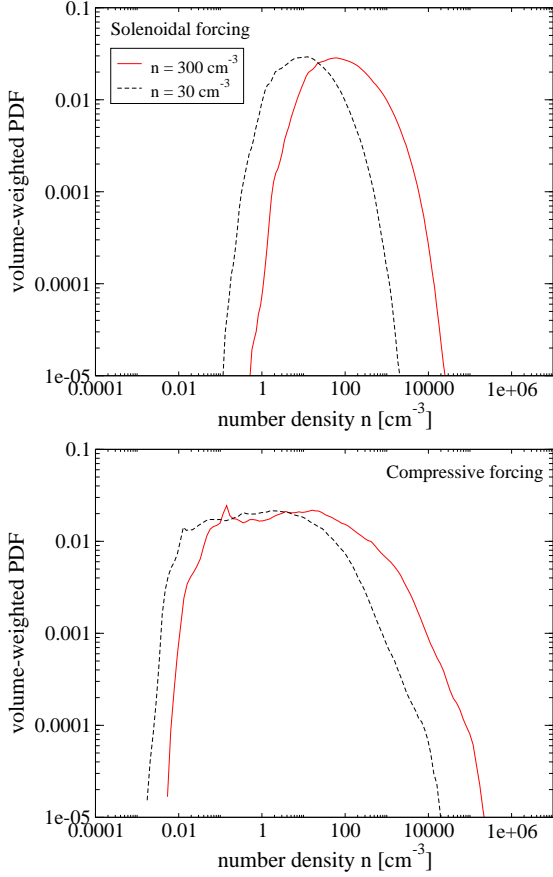


Figure 4. Volume-weighted density PDF for solenoidal (top) and compressive (bottom) forcing at time $t = 0.5$ crossing time in runs with $v_{\text{rms}} = 2 \text{ km s}^{-1}$. The red solid line presents the PDF in the run with mean density 300 cm^{-3} , while the black dashed line shows the PDF in the run with mean density 30 cm^{-3} .

therefore find a smaller difference between the H_2 formation rates in the solenoidal and compressive runs than one might expect given the significant difference in the density PDF.

In order to more quantitatively describe the H_2 distribution, we examine how the H_2 fraction varies with density. We compute x_{H_2} and n for each of the cells in the simulation volume and then bin the data by number density. We then compute the mean and standard deviation for x_{H_2} in each bin. The resulting values at $t = 0.5$ turbulent crossing times after the chemistry module is turned on are plotted in Figure 5. We clearly see a considerable scatter in the value of x_{H_2} at a given density. However, there is still an obvious underlying trend in the distribution of x_{H_2} with n , telling us that high density gas is more highly molecular, as expected (e.g. Hollenbach et al. 1971). At this point in the high density simulation the gas is almost fully molecular, whereas in the low density case $x_{\text{H}_2} \simeq 0.3$ for solenoidal and $x_{\text{H}_2} \simeq 0.7$ for compressive forcing (see Fig. 3). Despite this, however, there are regions where the H_2 fraction is already much higher, and we can see that gas with a number density $n > 10^3 \text{ cm}^{-3}$ is already almost entirely molecular in all of the simulations.

We also examine how the gas temperature varies as a function of number density in our simulations. Just as with the H_2 fraction above, we use the temperature output from

our runs, bin it by number density n , and then compute the mean temperature and the standard deviation in the mean for each bin. We plot the resulting values again at $t = 0.5$ turbulent crossing time in Figure 6. Strong shocks present in the turbulent simulations lead to high post-shock temperatures that can reach several thousand Kelvin. In low density gas, these shocks cause a significant scatter in the temperatures. In high density gas, their effect is less pronounced, owing to the significantly shorter cooling time. In the case of compressive forcing, the gas is found to have a wider range of densities than the gas in the case of solenoidal forcing. As discussed before, this is a result of the stronger compressions produced by the turbulent forcing.

A final notable feature in the temperature distributions is the fact that in the low density solenoidal run, the temperature of the gas at $\log n \geq 3.5$ is clearly higher than in the other runs. This occurs because in this run, there is still a significant quantity of atomic hydrogen present at these densities (see Fig. 5), allowing heating due to H_2 formation to contribute significantly to the thermal balance of the gas. In the other runs, the atomic hydrogen fraction at these densities is very much smaller, and H_2 formation heating does not play a significant role in determining the gas temperature.

3.3 Dependence on the density clumping factor

As we are using periodic boundary conditions in our simulations, which prevent any of the H_2 molecules that form from escaping from the simulation volume, it is relatively straightforward to show that the evolution of the mass-weighted mean H_2 abundance with time is described by the following equation

$$\frac{d\langle x_{\text{H}_2} \rangle_{\text{M}}}{dt} = \langle 2R_{\text{H}_2}(T, T_{\text{d}})x_{\text{H}}n - D_{\text{H}_2}x_{\text{H}_2}n \rangle_{\text{M}}, \quad (10)$$

where $R_{\text{H}_2}(T, T_{\text{d}})$ is the rate coefficient for H_2 formation on dust grains (reaction 1), and D_{H_2} is a destruction term depending on both temperature and density that accounts for the loss of H_2 in reactions 3, 4, 6 and 7 in Table 1. In practice, the impact of this destruction term is very small, unless $x_{\text{H}} \ll x_{\text{H}_2}$, and so to a good approximation

$$\frac{d\langle x_{\text{H}_2} \rangle_{\text{M}}}{dt} \simeq \langle 2R_{\text{H}_2}(T, T_{\text{d}})x_{\text{H}}n \rangle_{\text{M}}. \quad (11)$$

As it stands, Eq. 11 is not particularly useful, as in order to solve for the time dependence of $\langle x_{\text{H}_2} \rangle_{\text{M}}$, we need to know how R_{H_2} , x_{H} , and n are correlated, and how this correlation evolves with time. However, we can convert Equation 11 to a more useful form if we make a few further approximations. First, when the fractional ionization of the gas is small, as it is throughout our simulations, we have $x_{\text{H}} \simeq 1 - x_{\text{H}_2}$, and hence

$$\frac{d\langle x_{\text{H}_2} \rangle_{\text{M}}}{dt} \simeq \langle 2R_{\text{H}_2}(T, T_{\text{d}})(1 - x_{\text{H}_2})n \rangle_{\text{M}}. \quad (12)$$

Second, in our simulations we keep the dust temperature fixed, and we know that most of the gas has a temperature that lies within the fairly narrow range of $10 - 40 \text{ K}$ (see Fig. 6). As the dependence of $R_{\text{H}_2}(T, T_{\text{d}})$ on T is weak when the temperature is low, we do not introduce a large error by treating the gas temperature (and hence R_{H_2}) as if

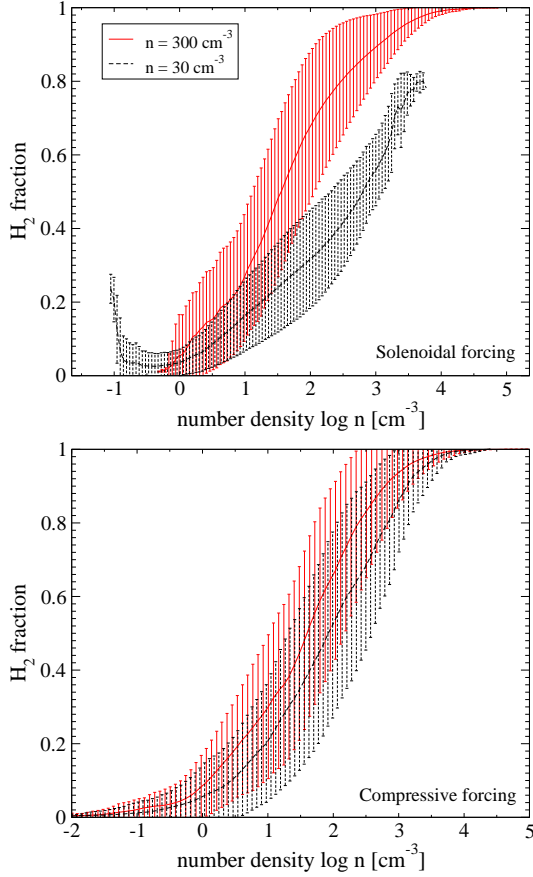


Figure 5. Mean H_2 fraction, plotted as a function of the number density n of the gas at time $t = 0.5$ crossing time in runs with $v_{\text{rms}} = 2 \text{ km s}^{-1}$ that use solenoidal (top) and compressive (bottom) forcing. The red solid line indicates the runs with mean density $n_0 = 300 \text{ cm}^{-3}$, and the black dashed line indicates the runs with mean density $n_0 = 30 \text{ cm}^{-3}$. To compute these values, we binned the data by number density and computed the mean value of x_{H_2} for each bin. The standard deviation in the value of x_{H_2} in each bin is indicated by the error bars.

it were uncorrelated with the density, allowing us to write Equation 12 as

$$\frac{d\langle x_{\text{H}_2} \rangle_{\text{M}}}{dt} \simeq 2R_{\text{H}_2}(\langle T \rangle_{\text{M}}, T_{\text{d}})\langle (1 - x_{\text{H}_2})n \rangle_{\text{M}}, \quad (13)$$

where $\langle T \rangle_{\text{M}}$ is the mass-weighted mean temperature.

To proceed further, it is necessary to make an additional assumption regarding the correlation between the H_2 fraction and the density. Given the presence of the turbulence, it is appealing to assume that this turbulence perfectly mixes the gas on a timescale much shorter than the chemical timescale. If we make this assumption, then we can treat x_{H_2} as being uncorrelated with density, allowing us to rewrite Equation 13 as

$$\frac{d\langle x_{\text{H}_2} \rangle_{\text{M}}}{dt} = 2R_{\text{H}_2}(\langle T \rangle_{\text{M}}, T_{\text{d}})\langle (1 - x_{\text{H}_2}) \rangle_{\text{M}} \langle n \rangle_{\text{M}} \quad (14)$$

$$= 2R_{\text{H}_2}(\langle T \rangle_{\text{M}}, T_{\text{d}})(1 - \langle x_{\text{H}_2} \rangle_{\text{M}})C_n \langle n \rangle_{\text{V}}, \quad (15)$$

where $\langle n \rangle_{\text{V}}$ is the volume-weighted mean of n , defined as

$$\langle n \rangle_{\text{V}} \equiv \frac{1}{V} \int_V n dV. \quad (16)$$

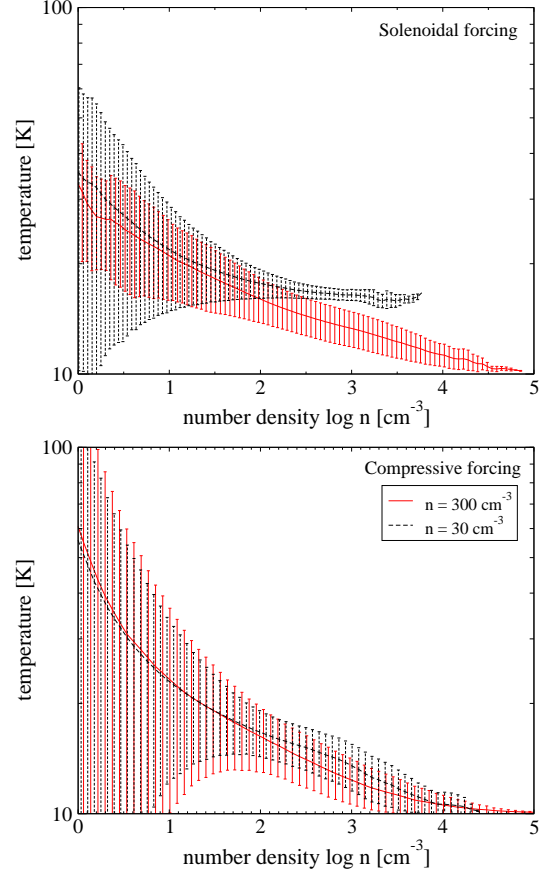


Figure 6. Mean gas temperature plotted as a function of the number density n at time $t = 0.5$ crossing time in runs with $v_{\text{rms}} = 2 \text{ km s}^{-1}$ using solenoidal (top) and compressive (bottom) forcing. The red solid line indicates the run with mean density of 300 cm^{-3} and the black dashed line indicates the run with mean density of 30 cm^{-3} . The data were binned in a similar fashion as for Figure 5. The standard deviation in the mean value in each bin is also indicated.

This quantity is related to the mass-weighted mean of n by

$$\langle n \rangle_{\text{M}} = \frac{1}{M} \int_V \rho n dV, \quad (17)$$

$$= \frac{1.4m_{\text{H}}}{M} \int_V n^2 dV, \quad (18)$$

$$= \frac{1.4m_{\text{H}}}{1.4m_{\text{H}}\langle n \rangle_{\text{V}}V} \langle n^2 \rangle_{\text{V}}, \quad (19)$$

$$= C_n \langle n \rangle_{\text{V}}, \quad (20)$$

where $C_n \equiv \langle n^2 \rangle_{\text{V}} / \langle n \rangle_{\text{V}}^2$ is the density clumping factor, and where we have used the fact that $\rho = 1.4m_{\text{H}}n$, and hence that $M \equiv \langle \rho \rangle_{\text{V}}V = 1.4m_{\text{H}}\langle n \rangle_{\text{V}}V$.

Equation 15 demonstrates that if our assumption of rapid mixing of the H_2 were true, then the evolution of the mass-weighted mean H_2 fraction in a gas cloud would be related in a very simple fashion to the mean density of the cloud and its density clumping factor. This fact has been used by Gnedin et al. (2009) as the basis of a simple sub-grid scale model of H_2 formation for cosmological simulations, or for other large-scale simulations without sufficient resolution to model the small-scale structure within molecular clouds. They write the formation rate of H_2 in a similar

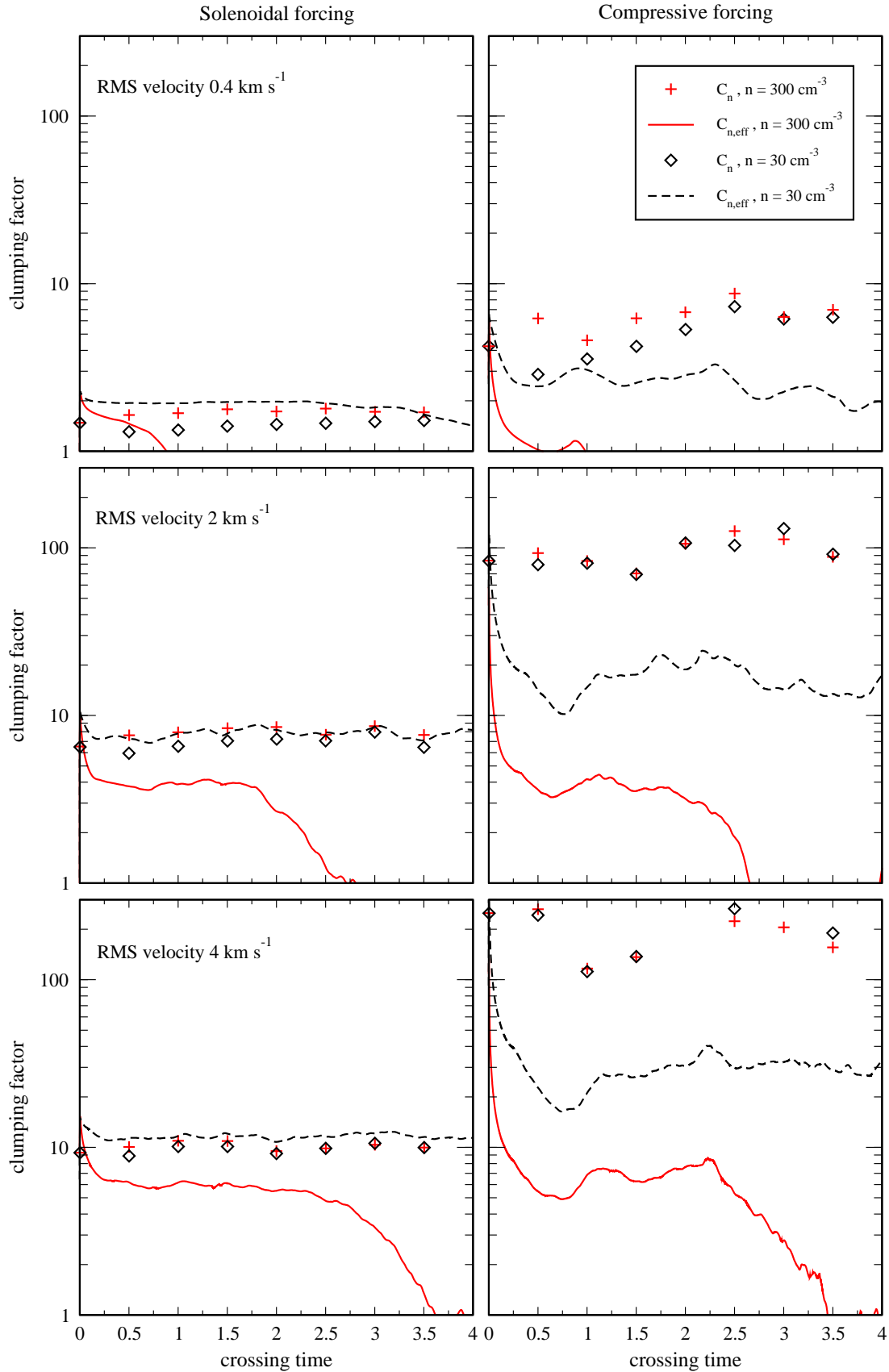


Figure 7. Evolution of the effective clumping factor $C_{n,\text{eff}}$ (lines) and the true clumping factor C_n (symbols) as a function of the turbulent crossing time T in runs with mean densities of 30 cm^{-3} (black) and 300 cm^{-3} (red). We plot results for three different values of the rms turbulent velocity: 0.4 km s^{-1} (top), 2 km s^{-1} (middle) and 4 km s^{-1} (bottom). The left-hand panels show the results for purely solenoidal forcing, while the right-hand panels show the results for purely compressive forcing.

form to Eq. 15, and argue that $C_n \sim 3\text{--}10$ in typical turbulent clouds. Gnedin & Kravtsov (2011) further developed this idea, and showed that this sub-grid model does a good job of reproducing the dependence of the average atomic and molecular gas surface densities on the total hydrogen surface density that is observed in nearby spiral galaxies (Wong & Blitz 2002), and the dependence of the mean H_2 fraction on the total hydrogen column density observed in our own Galaxy (Gillmon et al. 2006; Wolfire et al. 2008).

However, the fact that we see a clear correlation between x_{H_2} and n in our simulations (see Fig. 5) implies that the assumption of rapid mixing that we used to derive Equation 15 is incorrect. In reality, it takes roughly one-third of a turbulent crossing time to fully mix material from overdense clumps into their lower density surroundings for solenoidal turbulence (Federrath et al. 2008a), and potentially longer than this for compressive turbulence. Therefore, a prescription such as that in Eq. 15 will overestimate the H_2 formation rate.

Our present simulations of solenoidal and compressive turbulence provide a useful test-bed for quantifying the extent to which Eq. 15, and by extension the Gnedin et al. sub-grid model, overestimates the H_2 formation rate. To do this, we define an ‘effective’ density clumping factor

$$C_{n,\text{eff}} = \frac{d\langle x_{\text{H}_2} \rangle_{\text{M}}/dt}{2R_{\text{H}_2}(\langle T \rangle_{\text{M}}, T_{\text{d}})(1 - \langle x_{\text{H}_2} \rangle_{\text{M}}\langle n \rangle_{\text{V}})}, \quad (21)$$

and compute how it evolves with time in each of our simulations, using our results for $\langle x_{\text{H}_2} \rangle_{\text{M}}$ and $\langle T \rangle_{\text{M}}$ discussed earlier. We then compare this with the true density clumping factor C_n computed at a number of different times during the simulations. The results of this comparison are plotted in Figure 7 (which shows the evolution between 0 and 4 crossing times) and Figure 8 (which shows an expanded view of the first 0.5 crossing times).

We see that at the very earliest times in the runs, there is a reasonable level of agreement between our inferred effective clumping factor $C_{n,\text{eff}}$ and the measured clumping factor C_n . Our computed values of $C_{n,\text{eff}}$ are typically some 20–40% larger than C_n , but an error of this magnitude is plausibly explained by our use of the mass-weighted mean temperature in our calculation of R_{H_2} : in reality, the dense gas, whose contribution initially dominates the H_2 formation rate, will generally be colder than this mean temperature.

However, this initial level of agreement between $C_{n,\text{eff}}$ and C_n is very quickly lost in most of the runs. In all of the simulations, the true clumping factor C_n remains approximately constant, varying by at most a factor of two in the compressive case, and by much less than this in the solenoidal case. On the other hand, in most of the runs, $C_{n,\text{eff}}$ decreases rapidly with time; only in the low density solenoidal model it does remain approximately constant during the lifetime of the simulation. The strong and almost immediate decrease of the effective clumping factor visible in Figures 7 and 8 is caused by the increase in the H_2 abundance in the dense gas. As the dense regions that initially dominate the H_2 formation rate become almost fully molecular, their contribution decreases rapidly, causing a significant fall in the mean H_2 formation rate within the simulation, and hence a significant decrease in $C_{n,\text{eff}}$. This effect is particularly pronounced in the compressively-forced runs, owing to their broad density PDFs. If we closely compare the results

plotted in Figure 8 with the time evolution of the H_2 fraction shown in Figure 3, we can see that the Gnedin et al. (2009) approach starts to break down when the gas is about 30% molecular. In the high density solenoidal runs, the H_2 formation rate is almost immediately overestimated by a factor of 2, while in the compressive runs, the rate is overestimated by a factor of 4 in the low density case, and by a factor of 10 in the high density case.

It is clear from this analysis that in most cases there is no simple way to relate the mean number density of the gas and the current mass-weighted mean H_2 abundance to the current H_2 formation rate, given the strong time variation that we see in $C_{n,\text{eff}}$. This time variation is absent only when the characteristic H_2 formation timescale is longer than a turbulent crossing time, as is the case in our low-density solenoidal runs, as only in this case is our assumption of rapid turbulent mixing justified. One must therefore be careful when using the Gnedin et al. (2009) sub-grid model to describe the H_2 formation rate in numerical simulations.

4 SUMMARY

We have presented the results of a study of H_2 formation in the turbulent ISM that examines the influence of the amplitude and mode of both solenoidal and compressive turbulent driving. We have performed high-resolution 3D hydrodynamic simulations using the massively parallel code FLASH, which we have modified to include a detailed treatment of atomic/molecular cooling and the most important hydrogen chemistry. Even though the chemical network we use is significantly simplified compared to the most detailed models available, it performs with acceptable accuracy for our purposes. We have performed simulations with numerical resolutions of 128^3 , 256^3 and 512^3 zones, and have demonstrated that our results are well-converged in our 256^3 runs. Our results also serve as a proof-of-concept application for our implementation of our non-equilibrium chemical model within the FLASH adaptive mesh refinement code.

We find that with both compressively and solenoidally driven turbulence, molecular hydrogen forms faster in gas with a higher mean density, or an environment with stronger turbulence. Although initially (during the first million years), H_2 formation is significantly faster with compressive turbulence than with solenoidal turbulence, at later times the differences become smaller, with the time taken to reach a molecular hydrogen fraction of 90% varying by at most a factor of three between the compressive and solenoidal runs. In almost all of our simulations, the gas becomes highly molecular within a much shorter time than the 10–20 Myr that would plausibly be required to assemble the cloud from the diffuse ISM (Ballesteros-Paredes, Hartmann & Vázquez-Semadeni 1999; Elmegreen 2000; Hartmann et al. 2001).

We have also shown that when time is measured in the units of turbulent crossing time, the H_2 formation timescale becomes much less dependent on the strength of the turbulence. Increasing the strength of the turbulence produces more dense gas and reduces the time taken to form H_2 . However, it also reduces the turbulent crossing time of the gas. In the solenoidal case, the reduction in the turbulent crossing time is the dominant effect, and so H_2 formation takes

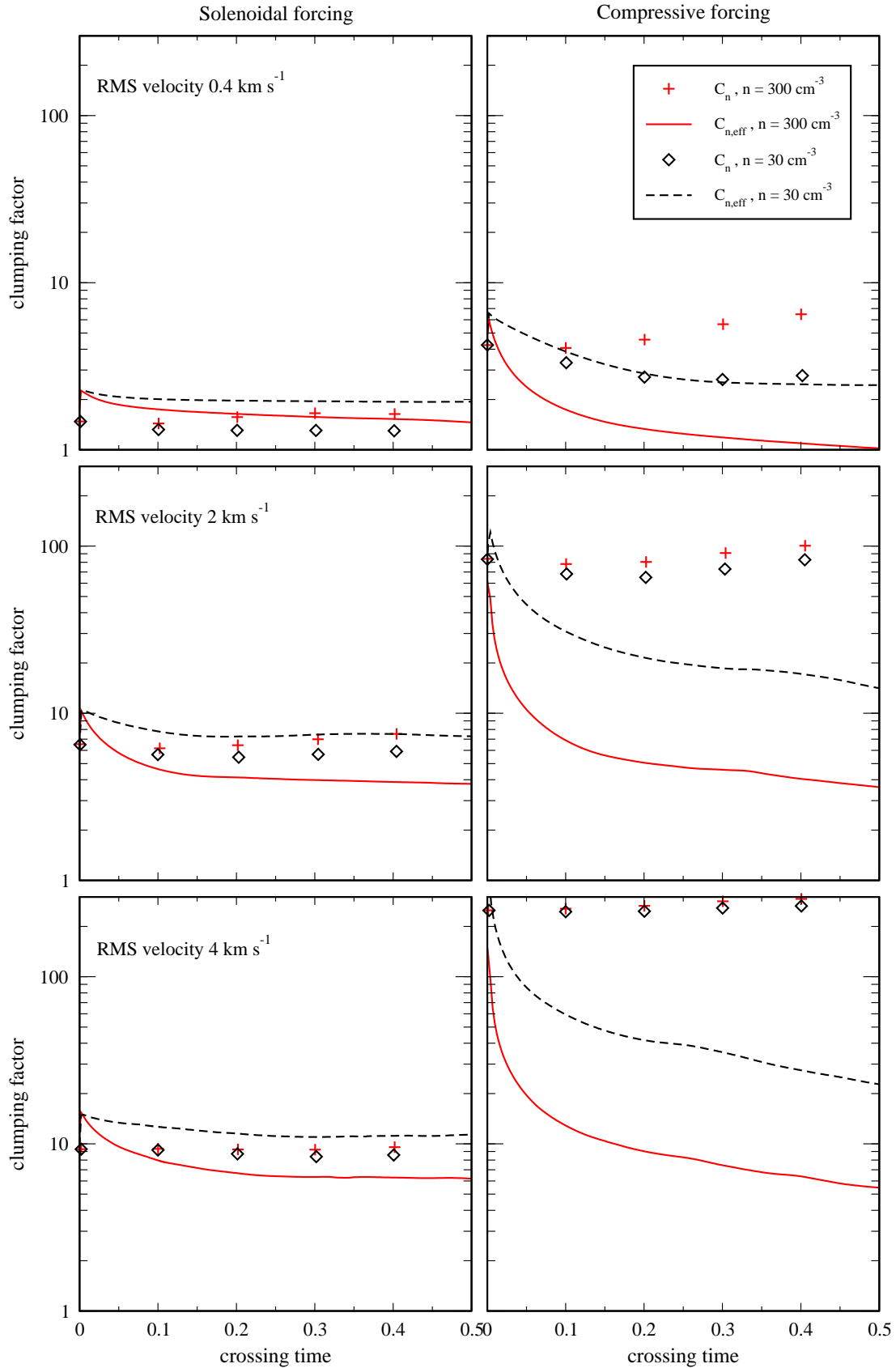


Figure 8. As Figure 7, but showing an expanded view of the first 0.5 crossing times. As before, three different values of the rms turbulent velocity v_{rms} are considered: 0.4 km s^{-1} (top), 2 km s^{-1} (middle) and 4 km s^{-1} (bottom) - and two different mean densities - 30 cm^{-3} (black) and 300 cm^{-3} (red). The left-hand panels show the results for purely solenoidal forcing, while the right-hand panels show the results for purely compressive forcing.

longer (in units of the crossing time) as we increase v_{rms} . On the other hand, in the compressive case, the broadening of the density PDF is the dominant effect, and increasing v_{rms} leads to a moderate decrease in the H_2 formation timescale measured in units of the crossing time.

The differences we have found between the compressive and solenoidal runs can largely be understood by considering the differences in the density PDFs in Figure 4. Compressive forcing produces a much wider spread of densities than solenoidal forcing, and since the H_2 formation rate per unit volume scales almost linearly with density when x_{H_2} is small, this allows the compressive runs to form H_2 much more rapidly at early times. However, rapid H_2 formation in the dense gas leads to its conversion to fully molecular form, at which point it no longer contributes to the total H_2 formation rate. This phenomenon occurs in both the solenoidal and the compressive runs, but has a greater effect in the compressive runs owing to the faster initial H_2 formation rate in these runs.

Finally, we have also used the results of our study to show that the Gnedin et al. (2009) prescription for correcting for the influence of unresolved density fluctuations on the H_2 formation rate in large-scale Galactic or cosmological simulations must be used with caution. The Gnedin et al. (2009) prescription assumes rapid gas mixing, when in reality it takes about one-third of a turbulent crossing time to mix the material from overdense clumps into the low density regions in the case of solenoidal forcing, and possibly even longer in the case of compressively-driven turbulence (Federrath et al. 2008a). We have shown that the effective clumping factor calculated with the assumption of rapid mixing over-predicts the H_2 formation rate. In the case of high density and strong compressive forcing, the H_2 formation rate can be overestimated by more than an order of magnitude at all but the very earliest times. For applications where one simply wants to determine which regions of the ISM become H_2 -dominated (i.e. more than 50% molecular) and how quickly this occurs, their approach remains reasonably accurate, since $C_{n,\text{eff}}$ shows little variation while $\langle x_{\text{H}_2} \rangle_{\text{M}}$ remains small. On the other hand, if one is interested in the final, equilibrium state of the gas (as in e.g. Krumholz & Gnedin 2010), then this approach may be problematic, as it will systematically over-predict the H_2 formation rate in highly molecular regions, with the result that the H_2 abundance will reach equilibrium too rapidly.

ACKNOWLEDGMENTS

We thank M.-M. Mac Low, S. Walch, and M. Wolfire for interesting discussions and valuable comments on the present work. We thank the anonymous referee for insightful comments. M.M. acknowledges financial support by the International Max Planck Research School for Astronomy and Cosmic Physics at the University of Heidelberg (IMPRS-HD) and the Heidelberg Graduate School of Fundamental Physics (HGSFP). The HGSFP is funded by the Excellence Initiative of the German Research Foundation DFG GSC 129/ 1. C.F. has received funding from the European Research Council under the European Community's Seventh Framework Programme (FP7/2007-2013 Grant Agreement no. 247060) for the research presented in

this work. S.C.O.G., C.F., and R.S.K. acknowledge financial support from the *Baden-Württemberg Stiftung* via the program International Collaboration II (grant P-LS-SPII/18) and from the German *Bundesministerium für Bildung und Forschung* via the ASTRONET project STAR FORMAT (grant 05A09VHA). R.S.K. furthermore gives thanks for subsidies from the *Deutsche Forschungsgemeinschaft* under grants no. KL 1358/1, KL 1358/4, KL 1359/5, KL 1358/10, and KL 1358/11, as well as from a Frontier grant of Heidelberg University sponsored by the German Excellence Initiative. The simulations used computational resources from the HLRBII project pr32hu at Leibniz Rechenzentrum Garching. The software used in this work was in part developed by the DOE-supported ASC/Alliance Center for Astrophysical Thermonuclear Flashes at the University of Chicago.

REFERENCES

- Abel, T., Anninos, P., Zhang, Y., Norman, M. L., 1997, *New Astron.*, 2, 181
- Ballesteros-Paredes J., Hartmann L., Vázquez-Semadeni E., 1999, *ApJ*, 527, 285
- Boley, A. C., Hartquist, T. W., Durisen, R. H., Michael, S., 2007, *ApJ*, 656, L89
- Brown P. N., Byrne G. D., Hindmarsh A. C., 1989, *SIAM J. Sci. Stat. Comput.*, 10, 1038
- Brunt, C. M., 2010, *A&A*, 513, 67
- Brunt, C. M., Heyer, M. H., Mac Low, M.-M., 2009, *A&A*, 504, 883
- Calder, A. C., Fryxell, B., Plewa, T., et al., 2002, *ApJS*, 143, 201
- Colella, P., Woodward, P. R., 1984, *Journal of Computational Physics*, 54, 174
- Elmegreen B. G., 2000, *ApJ*, 530, 277
- Elmegreen B. G., Scalo J., 2004, *ARA&A*, 42, 211
- Falgarone, E., Puget, J. L., Perault, M., 1992, *A&A*, 257, 715
- Federrath, C., Glover, S. C. O., Klessen, R. S., Schmidt, W., 2008a, *Phys. Scr. T*, 132, 014025
- Federrath, C., Klessen, R. S., Schmidt, W., 2008b, *ApJ*, 688, L79
- Federrath, C., Klessen, R. S., Schmidt, W., 2009, *ApJ*, 692, 364
- Federrath C., Roman-Duval J., Klessen R., Schmidt W., Mac Low M.-M., 2010, *A&A*, 512, 81
- Ferland, G. J., Peterson, B. M., Horne, K., Welsh, W. F., Nahar, S. N., 1992, *ApJ*, 387, 95
- Fryxell, B., Olson, K., Ricker, P., et al., 2000, *ApJS*, 131, 273
- Gillmon, K., Shull, J. M., Tumlinson, J., Danforth, C., 2006, *ApJ*, 636, 891
- Glover, S. 2003, *ApJ*, 584, 331
- Glover, S. C. O., Abel, T., 2008, *MNRAS*, 388, 1627
- Glover, S. C. O., Clark, P. C., 2011a, *MNRAS*, in press: arXiv:1102.0670
- Glover, S. C. O., Clark, P. C., 2011b, *MNRAS*, in press: arXiv:1105.3073
- Glover, S. C. O., Mac Low, M.-M., 2007a, *ApJS*, 169, 239
- Glover, S. C. O., Mac Low, M.-M., 2007b, *ApJ*, 659, 1317
- Glover, S. C. O., Federrath, C., Mac Low, M.-M., Klessen, R. S., 2010, *MNRAS*, 404, 2

Glover, S. C. O., Mac Low, M.-M., 2011, MNRAS, 412, 337
 Gnedin, N. Y., Tassis, K., Kravtsov, A. V., 2009, ApJ, 697, 55
 Gnedin, N. Y., Kravtsov, A., 2011, ApJ, 728, 88
 Goldreich, P., Kwan, J., 1974, ApJ, 191, 93
 Goldsmith, P. F., Langer, W. D., 1978, ApJ, 222, 881
 Gould, R. J., Salpeter, E. E., 1963, ApJ, 138, 393
 Hartmann, L., Ballesteros-Paredes, J., & Bergin, E. A., 2001, ApJ, 562, 852
 Heyer, M. H., Brunt, C. M., 2004, ApJ, 615, L45
 Hollenbach, D., McKee, C. F., 1979, ApJS, 41, 555
 Hollenbach, D., McKee, C. F., 1989, ApJ, 342, 306
 Hollenbach, D., Werner, M. W., Salpeter, E. E., 1971, ApJ, 163, 165
 Klessen, R. S., 2001, ApJ, 556, 837
 Klessen, R. S., Heitsch, F., Mac Low, M.-M., 2000, ApJ, 535, 887
 Krumholz, M. R., & Gnedin, N. Y. 2010, ApJ, accepted; arXiv:1011.4065
 Krumholz, M. R., McKee, C. F., Tumlinson, J., 2009, ApJ, 693, 216
 Larson, R. B., 1981, MNRAS, 194, 809
 Lemaster, M. N., Stone, J. M., 2008, ApJ, 682, L97
 Mac Low, M.-M., Klessen, R. S., Burkert, A., & Smith, M. D. 1998, Phys. Rev. Lett., 80, 2754
 Mac Low, M.-M. 1999, ApJ, 524, 169
 Mac Low, M.-M., Glover, S. C. O., 2011, ApJ, in press; arXiv:1011.3054
 Mac Low, M.-M., Klessen, R. S., 2004, Rev. Mod. Phys., 76, 125
 Mac Low, M.-M., Shull, J. M., 1986, ApJ, 302, 585
 Martin, P. G., Keogh W. J., Mandy, M. E., 1998, ApJ, 499, 793
 Myers, P. C., 1983, ApJ, 270, 105
 Ossenkopf, V., Mac Low, M.-M., 2002, A&A, 390, 307
 Ostriker, E. C., Stone, J. M., Gammie, C. F., 2001, ApJ, 546, 980
 Pérault, M., Falgarone, E., Puget, J. L., 1986, A&A, 157, 139
 Plewa, T., Müller, E., 1999, A&A, 342, 179
 Price, D. J., Federrath, C., 2010, MNRAS, 406, 1659
 Price, D. J., Federrath, C., Brunt, C. M., 2011, ApJ, 727, L21
 Roman-Duval, J., Federrath, C., Brunt, C., Heyer, M., Jackson, J., Klessen, R. S., 2011, ApJ, 740, 120
 Scalo J., Elmegreen B. G., 2004, ARA&A, 42, 275
 Schmidt, W., Federrath, C., Hupp, M., Kern, S., Niemeyer, J. C., 2009, A&A, 494, 127
 Schneider, N., Bontemps, S., Simon, R., Ossenkopf, V., Federrath, C., Klessen, R. S., Motte, F., Andr, Ph., Stutzki, J., Brunt, C., 2011, A&A, 529, 1
 Sembach, K. R., Howk, J. C., Ryans, R. S. I., Keenan, F. P., 2000, ApJ, 528, 310
 Solomon, P. M., Rivolo, A. R., Barrett, J., Yahil, A., 1987, ApJ, 319, 730
 Sutherland, R. S., Dopita, M. A., 1993, ApJS, 88, 253
 Trevisan, C. S., Tennyson, J., 2002, Plasma Phys. Controlled Fusion, 44, 1263
 Weingartner, J. C., Draine, B. T., 2001, ApJ, 563, 842
 Wolfire, M. G., McKee, C. F., Hollenbach, D., Tielens, A. G. G. M., 2003, ApJ, 587, 278

Wolfire, M. G., Tielens, A. G. G. M., Hollenbach, D., Kaufman, M. J., 2008, ApJ, 680, 384
 Wong, T., Blitz, L., 2002, ApJ, 569, 157
 Woodall, J., Agúndez, M., Markwick-Kemper, A. J., Millar, T. J., 2007, A&A, 466, 1197
 Zuckerman, B., Evans, N. J., II, 1974, ApJ, 192, 149

This paper has been typeset from a \LaTeX file prepared by the author.